ARTICLES
https://doi.org/10.1038/s41563-022-01277-3

nature materials

Check for updates

Imaging gate-tunable Tomonaga–Luttinger liquids in 1H-$MoSe_2$ mirror twin boundaries

Tiancong Zhu[1,2,11], Wei Ruan[1,2,3,11]✉, Yan-Qi Wang[1,2,11], Hsin-Zon Tsai[2], Shuopei Wang[4,5], Canxun Zhang[2,6], Tianye Wang[1,2], Franklin Liou[2,6], Kenji Watanabe[7], Takashi Taniguchi[8], Jeffrey B. Neaton[1,2], Alexander Weber-Bargioni[1,9], Alex Zettl[1,2,6], Z. Q. Qiu[1,2], Guangyu Zhang[4,5,10], Feng Wang[1,2,6]✉, Joel E. Moore[1,2,6]✉ and Michael F. Crommie[1,2,6]✉

One-dimensional electron systems exhibit fundamentally different properties than higher-dimensional systems. For example, electron–electron interactions in one-dimensional electron systems have been predicted to induce Tomonaga–Luttinger liquid behaviour. Naturally occurring grain boundaries in single-layer transition metal dichalcogenides exhibit one-dimensional conducting channels that have been proposed to host Tomonaga–Luttinger liquids, but charge density wave physics has also been suggested to explain their behaviour. Clear identification of the electronic ground state of this system has been hampered by an inability to electrostatically gate such boundaries and tune their charge carrier concentration. Here we present a scanning tunnelling microscopy and spectroscopy study of gate-tunable mirror twin boundaries in single-layer 1H-$MoSe_2$ devices. Gating enables scanning tunnelling microscopy and spectroscopy for different mirror twin boundary electron densities, thus allowing precise characterization of electron–electron interaction effects. Visualization of the resulting mirror twin boundary electronic structure allows unambiguous identification of collective density wave excitations having two velocities, in quantitative agreement with the spin–charge separation predicted by finite-length Tomonaga–Luttinger liquid theory.

Reduced screening, enhanced quantum fluctuations and confinement effects in one-dimensional electron systems (1DESs) cause a variety of exotic phenomena such as quantum spin liquids[1], Peierls transitions[2], single electron transport[3] and Tomonaga–Luttinger liquids (TLLs)[4–21]. Some important characteristics of TLLs include power-law conductance and spin–charge separation, both of which depend sensitively on the ratio of electron–electron (el-el) interaction strength to electron kinetic energy. Spin–charge separation[15,16,19–21] and el-el interaction strength[12,22] have been characterized in various 1DESs, but such measurements have led to inconsistent TLL parameters when measured within the same 1DES, suggesting that other physical mechanisms might be at play in the samples studied. Recently discovered mirror twin boundaries (MTBs) in single-layer (SL) 1H-MoX_2 (X = S, Se, Te) provide a new system in which to explore such behaviour. These MTBs form a one-dimensional (1D) metallic channel within a two-dimensional semiconducting bulk that is ideal for investigating interacting electronic behaviour in 1DESs having atomic-scale feature size and varying length[23]. Signatures of an energy gap (rather than a power-law density of states[12–14]) and charge density modulations have been experimentally demonstrated[23–30] in MTBs, consistent with theoretical predictions for a finite-length TLL[31–36], but debate exists as to whether their origin might rather be due to a Peierls instability[23–26,28]. Some spectroscopic evidence of spin–charge separation in MTBs has been observed[27], but clear identification of the spin/charge velocities and direct comparison of these properties to the MTB el-el interaction strength are still missing.

Here we report the observation of finite-length TLL behaviour for MTBs embedded in gate-tunable SL 1H-$MoSe_2$ devices and characterized by scanning tunnelling microscopy/spectroscopy (STM/STS). While an earlier published measurement of MTB electronic structure involved non-gate-tunable samples of SL 1H-$MoSe_2$ and was interpreted as evidence for charge density wave behaviour[24], our gate-tunable MTB devices provide a remarkable experimental advancement over this and yield important insights that suggest a different type of MTB behaviour (that is, that MTBs exhibit a TLL ground state). The reason for this is that gating MTBs allows their carrier density to be tuned and enables unambiguous measurement of the MTB el-el interaction strength and carrier-density-dependent electronic structure. We observe strong variation in the MTB energy gap and charge density distribution as a function of applied gate voltage, consistent with expectations for a 1D particle in a box with interaction-induced level splitting. Clear evidence for TLL-based spin–charge separation in MTBs was obtained through measurement of two distinct spectral function modulations that correspond to collective spin and charge excitations with different dispersions. The characteristic TLL parameter obtained from the observed spin and charge velocities was found to be in excellent agreement with the separately measured MTB el-el interaction energy and energy-level spacing. Observation of such good agreement between

[1]Materials Sciences Division, Lawrence Berkeley National Laboratory, Berkeley, CA, USA. [2]Department of Physics, University of California, Berkeley, CA, USA. [3]State Key Laboratory of Surface Physics and Department of Physics, Fudan University, Shanghai, China. [4]Beijing National Laboratory for Condensed Matter Physics, Key Laboratory for Nanoscale Physics and Devices, Institute of Physics, Chinese Academy of Sciences, Beijing, China. [5]Songshan Lake Materials Laboratory, Dongguan, China. [6]Kavli Energy Nano Sciences Institute, University of California Berkeley and Lawrence Berkeley National Laboratory, Berkeley, CA, USA. [7]Research Center for Functional Materials, National Institute for Materials Science, Tsukuba, Japan. [8]International Center for Materials Nanoarchitectonics, National Institute for Materials Science, Tsukuba, Japan. [9]Molecular Foundry, Lawrence Berkeley National Laboratory, Berkeley, CA, USA. [10]School of Physical Sciences, University of Chinese Academy of Sciences, Beijing, China. [11]These authors contributed equally: Tiancong Zhu, Wei Ruan, Yan-Qi Wang. ✉e-mail: weiruan@fudan.edu.cn; fengwang76@berkeley.edu; jemoore@berkeley.edu; crommie@berkeley.edu

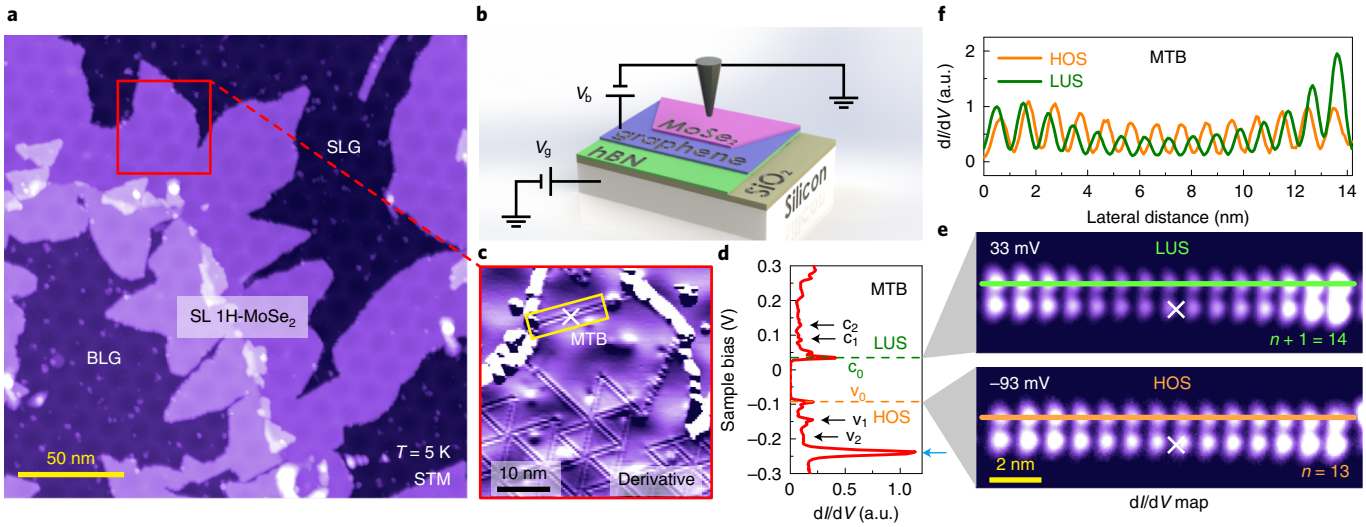

Fig. 1 | STM characterization of a SL $MoSe_2$/graphene/hBN/SiO_2/Si device at temperature $T = 5$ K. a, Large-scale STM topography of a SL $MoSe_2$/graphene/hBN/SiO_2/Si device (set-point parameters: $V_{set} = -2$ V, $I_{set} = 10$ pA). Here, SLG refers to single-layer graphene, and BLG refers to bilayer graphene. **b**, Schematic of the experimental device set-up. V_b is the bias voltage applied between the sample and STM tip. **c**, A close-up STM derivative image of the MTBs in the area indicated by a red square in **a** (the derivative plot enhances the MTB image contrast). **d**, The dI/dV spectrum acquired on the MTB in the yellow rectangle in **c** at the position marked by a white cross ($V_{set} = -0.3$ V, $I_{set} = 100$ pA, $V_{mod} = 2$ mV. V_{mod} is the a.c. modulation voltage in dI/dV spectroscopy measurements.). The energy gap is bracketed by the HOS (v_0) and the LUS (c_0). Other 1D quantum well states are labelled with black arrows while a charging peak is labelled with a blue arrow. **e**, Constant-height dI/dV maps of the MTB in **c** taken at the LUS (top) and the HOS (bottom; $I_{set} = 100$ pA, $V_{mod} = 10$ mV). The HOS map exhibits 13 nodes (n) while the LUS map exhibits 14 nodes. **f**, LDOS line profiles of the MTB at the energies of both the LUS and the HOS, acquired along the orange and green lines in **e**.

these parameters within a single 1DES provides unusually strong support for identification of the ground state as a TLL.

SL 1H-$MoSe_2$ was grown via molecular beam epitaxy (MBE) at the surface of epitaxial graphene supported by hexagonal boron nitride (hBN)/SiO_2/Si (Fig. 1a and Supplementary Fig. 1). This heterostructure arrangement allows systematic control of electron filling at the $MoSe_2$ surface by way of a doped Si bottom gate (Fig. 1b). The device was characterized by STM topographic imaging (Fig. 1a), which shows large SL $MoSe_2$ islands as well as a moiré superlattice formed by alignment of the graphene and hBN[37]. Isolated MTBs and MTB networks are seen as double-straight-line features that exhibit a 4|4P structure (4|4P refers to grain boundary structures composed of four-fold rings with point sharing between the rings) as reported previously[23,24] (Fig. 1c).

The electronic properties of an isolated 14-nm-long MTB (outlined in yellow in Fig. 1c) were characterized by measuring bias-dependent (V-dependent) STM differential conductance (dI/dV), which reflects the surface electronic local density of states (LDOS). Figure 1d shows a typical dI/dV spectrum at zero gate voltage ($V_g = 0$) that is consistent with previous measurements[24]. Three dominant features in the dI/dV spectrum can be identified: an energy gap of $\Delta_0 \approx 128$ meV bracketing the Fermi level (E_F; the peak-to-peak width between v_0 and c_0), additional peaks further out in energy from the gap (black arrows labelled by v_1, v_2, c_1, c_2) and a large peak at $V \approx -240$ meV (blue arrow).

The spatial distribution of MTB electronic states at different peak energies was characterized by performing constant-height dI/dV mappings of the MTB in Fig. 1c. Figure 1e shows the electronic LDOS of both the highest occupied state (HOS) at $V \approx -93$ meV (v_0) and the lowest unoccupied state (LUS) at $V \approx 33$ meV (c_0), revealing periodic charge modulations along the MTB, as well as a two-lobe spatial feature perpendicular to the MTB as seen previously[24,27,29]. The HOS is observed to have 13 nodes, whereas the LUS has 14, as seen from direct comparison of the LDOS line profiles (Fig. 1f) acquired along the orange and green lines in Fig. 1e (nodes here are defined as local minima in the interior of the MTB). A dI/dV map of the v_1 peak exhibits 12 nodes, while a map of the c_1 peak exhibits 15 nodes (Supplementary Fig. 2a–c), suggesting a particle-in-a-box nodal progression (that is, the number of nodes increases by 1 with each higher energy peak). The peaks v_i and c_i ($i \geq 0$) can thus be interpreted as representing confined quantum levels. Similar nodal structure was observed in all the MTBs studied here (Supplementary Fig. 3 for additional representative data).

To gain insight into the nature of the energy gap at E_F, we performed STS measurement of the MTB shown in Fig. 1c for different gate voltages in the range $-60\,\text{V} \leq V_g \leq 60\,\text{V}$, thus enabling the MTB to be tuned from the hole-doped regime ($V_g = -60$ V) to the electron-doped regime ($V_g = 60$ V). Figure 2a shows the gate-dependent dI/dV curves acquired at the position marked in Fig. 1e, while Fig. 2b shows a dI/dV intensity plot for a finer set of gate voltages at the same position. A key observation here is that the gap size changes with gate voltage. The dI/dV spectrum at $V_g = -60$ V (Fig. 2a, orange) shows a large gap at E_F of $\Delta_{large} \approx 121$ meV that is similar to the gap Δ_0, observed at $V_g = 0$ V (Fig. 2a, red). The dI/dV spectrum at $V_g = 60$ V (Fig. 2a, blue), however, shows a substantially smaller gap of $\Delta_{small} \approx 70$ meV. The peaks at the gap edge of Δ_{small} are also observed to have reduced intensities compared to those bracketing Δ_{large}. As V_g increases from −60 V, the overall band structure shifts rigidly towards lower energies, consistent with the electrostatic influence of the bottom gate. For $V_g \approx 10$ V, a pronounced peak (blue arrow) appears at negative bias voltage and shifts to higher energies with increasing V_g, opposite to the overall lowering trend seen for the rest of the band structure. Such behaviour allows us to identify this peak as a tip-induced charging feature of the LUS (Supplementary Fig. 4 shows a representative real-space image of the charging-ring feature associated with this peak in another MTB)[38]. For $V_g \approx 20$ V both the charging peak and the LUS begin to cross E_F, resulting in a transition from the large energy gap to the smaller gap. For $V_g > 20$ V both the charging peak and the overall band structure continue to shift, as expected for increased electron

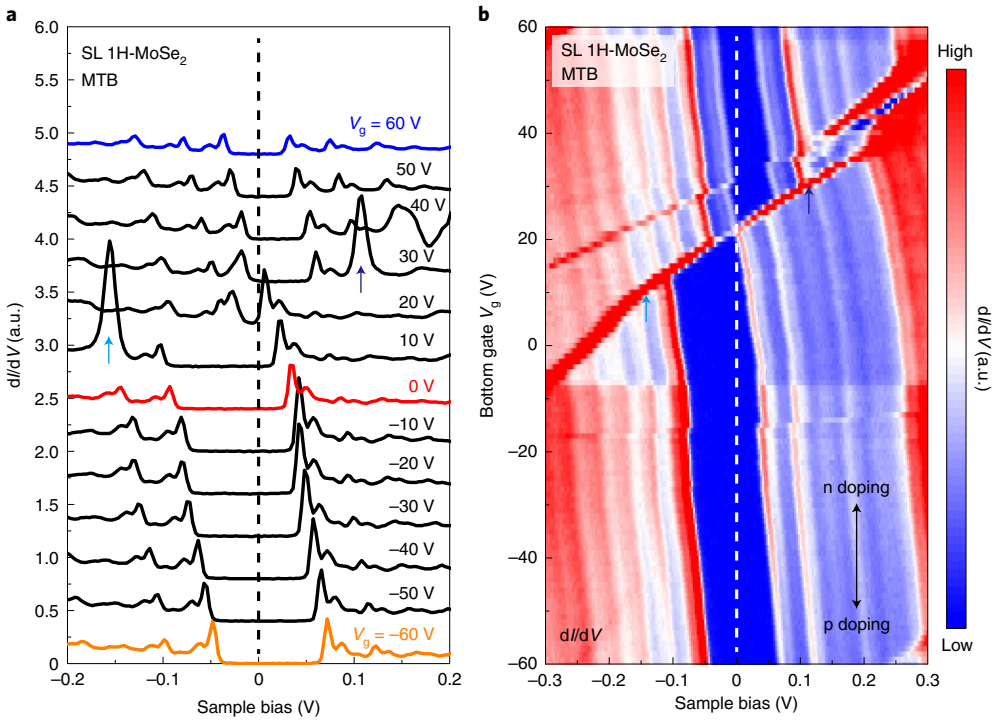

Fig. 2 | Gate-dependent electronic structure of the MTB. a, A waterfall plot showing dI/dV spectra acquired over the gate voltage range $-60\,V \leq V_g \leq 60\,V$ on the MTB from Fig. 1c ($V_{set} = -0.3\,V$, $I_{set} = 100\,pA$, $V_{mod} = 2\,mV$; position marked in Fig. 1c). The spectra exhibit a large energy gap for $V_g < 20\,V$ and a small gap for $V_g > 20\,V$. Electronic structure shifts to lower energy with increasing V_g (that is, with increased electron doping). The charging peaks are shown by the arrows. **b**, A density plot of dI/dV spectra acquired for $-60\,V \leq V_g \leq 60\,V$ on the MTB showing the overall band structure shift and energy gap transition as a function of V_g ($V_{set} = -0.3\,V$, $I_{set} = 100\,pA$, $V_{mod} = 5\,mV$; the slight reduction of intensity seen for $V_g \geq -8\,V$ arises from the fact that under this condition, a charging peak increases the tunnel current at the dI/dV set-point voltage and thereby causes a small retraction of the tip).

filling of the MTB. We note that a second charging peak can be seen (starting at $V_g = 15\,V$ and $V = -0.3\,V$ in Fig. 2b) that is possibly due to another MTB nearby. The influence of multiple charging peaks was mitigated by picking MTBs well isolated from others. Similar gate-dependent behaviour was also observed for 19 other MTBs that were similarly measured using a variety of different STM tips (Supplementary Fig. 5 for representative data).

Constant-height dI/dV maps of the HOS and LUS of the MTB in Fig. 1c at $V_g = \pm 60\,V$ further reveal gate-dependent real-space electronic structure (Fig. 3). The HOS and LUS for the large gap configuration at $V_g = -60\,V$ (Δ_{large}) exhibit 13 nodes and 14 nodes, respectively (Fig. 3b), consistent with the real-space electronic structure observed for the undoped ($V_g = 0\,V$) case (Fig. 1e,f). The HOS and LUS for the small gap configuration at $V_g = 60\,V$ (Δ_{small}), on the other hand, both exhibit 14 nodes (Fig. 3e). The LDOS maps of higher energy peaks are summarized in Supplementary Fig. 2d–i. (Similar gate-dependent nodal structure was observed for nine MTBs). This behaviour is in contrast to a Peierls instability in which out-of-phase spatial patterns are expected at the HOS and LUS[39].

In order to characterize the energy- and momentum-resolved MTB electronic structure, we measured dI/dV spectra along an MTB for the large gap case ($V_g = 0\,V$; Fig. 4a) and performed Fourier transform (FT) analysis of the resulting density plot (here we chose a longer MTB than that in Figs. 1–3 to achieve better momentum resolution). Figure 4b shows the energy dependence of the STS intensity plot as a function of the MTB axial coordinate (x axis) and the sample bias (y axis). Fast real-space modulations (wavelength $\lambda \approx 1\,nm$) create a complex MTB nodal structure that coexists with a longer wavelength modulation that induces a dome-shaped charge density profile (similar real-space modulations in electronic structure have been previously reported both for MTBs[19,21] and carbon nanotubes[15,16]).

Figure 4c shows the corresponding FT of the STS intensity plot, revealing both the energy dependence and momentum dependence of the electronic structure. Two linear dispersion branches with different slopes are seen to cross E_F at $q/2\pi \approx 1\,nm^{-1}$ (which we identify as $q = 2k_F$ where k_F is the Fermi wavevector) and are labelled by blue and red markers in Fig. 4c. These branches correspond to 'fast' real-space nodal structure and are dubbed the 'fast branches' hereafter. The velocity of the blue branch is $3.5 \times 10^5\,m\,s^{-1}$ (extracted from twice the slope of the dispersion since LDOS $\propto |\psi(x)|^2$, where $\psi(x)$ is the electron wavefunction) and is consistent with the Fermi velocity, v_F, of the MTB metallic band structure[24,27]. The velocity of the red branch, on the other hand, is $6.5 \times 10^5\,m\,s^{-1}$ and is higher than v_F. An additional linear branch near the Γ point (labelled by orange markers in Fig. 4c) can be resolved that corresponds to the long wavelength modulation mentioned above (and is dubbed the 'slow branch' hereafter). The existence of multiple linear dispersion branches causes blurring of the real-space nodal structure at peak energies far from E_F (Supplementary Fig. 3). A static mode (that is, constant wavevector with energy) at $q = 2k_F$ can also be observed, consistent with previous results[24]. Figure 4d provides a second-derivative plot of the data presented in Fig. 4c, which allows the various dispersive features to be more clearly seen. This type of behaviour was observed in all seven of the MTBs that were characterized in this way (Supplementary Figs. 6 and 7 for additional representative data). All the measured MTBs were well isolated from other MTBs and defects to avoid spatial inhomogeneities in the local electrostatic environment that might obscure the intrinsic MTB behaviour. We also calibrated our STM tip on a material (Au) with a work function close to that of $MoSe_2$ to minimize tip-induced band bending effects (tip-induced band bending can lead to 'curving'

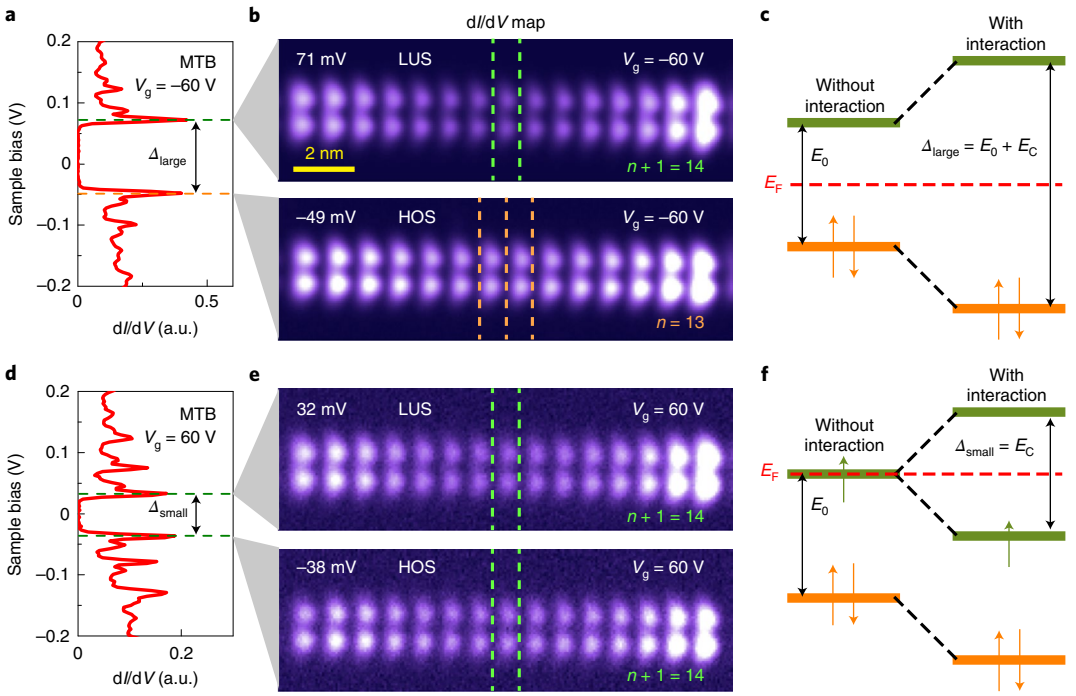

Fig. 3 | Electronic LDOS maps of states at gap edges for $V_g = -60$ V and $V_g = 60$ V. a, The d*I*/d*V* spectrum of the MTB in Fig. 1c taken at $V_g = -60$ V shows a large energy gap ($V_{set} = -0.3$ V, $I_{set} = 100$ pA, $V_{mod} = 2$ mV; position marked in Fig. 1c). **b**, Constant-height d*I*/d*V* maps of states at gap edges for $V_g = -60$ V ($V_{mod} = 10$ mV). The number of nodes for the HOS and the LUS differ by one. Green and orange dashed lines indicate the node positions of the corresponding wavefunctions. **c**, Energy-level diagram for the large energy gap case with and without el-el interactions. The arrows refer to electrons with up/down spin occupying the corresponding states. **d**, The d*I*/d*V* spectrum of the same MTB taken at $V_g = 60$ V shows a small energy gap ($V_{set} = -0.3$ V, $I_{set} = 100$ pA, $V_{mod} = 2$ mV; same position). **e**, Constant-height d*I*/d*V* maps of states at the gap edges for $V_g = 60$ V ($I_{set} = 100$ pA, $V_{mod} = 10$ mV). The number of nodes for the HOS and the LUS are now the same. **f**, Energy-level diagram for the small energy gap case with and without el-el interactions.

of the chemical potential with tip position due to local tip gating (Supplementary Figs. 6a and 8)).

Our experimental results are in excellent agreement with the theoretical predictions for a confined TLL. Our observation of gate-induced modulation of the energy gap size reveals that el-el Coulomb repulsion is a dominant factor in MTB electronic structure, a major characteristic of TLLs (the gate dependence of the gap size cannot be explained by screening effects or electron–phonon coupling; Supplementary Note 1 and Supplementary Fig. 9). Were el-el interactions absent, the Fermi level energy gap would be gate independent and would equal the 1D single-particle level spacing value of $E_0 = \hbar v_F \pi / L$ ($\hbar$ is the reduced Planck's constant; L is the length of the MTB). The presence of el-el Coulomb repulsion explains the large and small gap variation seen for different electron fillings since each MTB quantum confinement level has spin degeneracy and can accept two electrons. When only one of the spin states is filled by tuning the gate voltage, then el-el repulsion will create a charging gap $\Delta_{small} = E_C$ (E_C, charging energy) that is required to inject a second electron with opposite spin into the same MTB level, resulting in level splitting for electron addition versus removal and an overall magnetic ground state (Fig. 3f, green).

This charging behaviour explains the identical real-space nodal structure experimentally observed for the HOS and LUS in Fig. 3e, as well as the reduced spectral weight of the HOS and LUS states in Fig. 2 at $V_g = 60$ V (where the HOS and LUS both contain just a single spin state) compared to $V_g = -60$ V (where the HOS and LUS are both spin degenerate). When the MTB HOS level contains two electrons (for example, at $V_g = -60$ V) then repulsion between the HOS and LUS electrons adds E_C to the single-particle level spacing, E_0, resulting in a larger gap $\Delta_{large} = E_0 + E_C$ (Fig. 3c). In this case we expect a different number of nodes for the HOS and LUS since they are associated with different quantum confinement levels, as seen experimentally in Fig. 3b. This scenario is also supported by the fact that the single-particle level spacing defined by the energy difference between v_1 and the HOS (for example, $E_0 = 52$ meV (Fig. 1d)) matches the difference $\Delta_{large} - \Delta_{small} = 51$ meV (Fig. 2a), which comes from a different set of levels. Further evidence for this interpretation comes from the reentrant large–small–large gate-dependent gap size transition seen for some MTBs (Supplementary Fig. 5), which signals repeated filling/splitting of the confined energy levels.

Our observation of gate-induced modulation of the MTB energy gap allows a direct and precise measurement of E_C/E_0, the ratio of MTB el-el interaction energy to electron kinetic energy. Since the single-particle level spacing can be expressed as $E_0 = \hbar v_F \pi / L$ and the charging energy E_C is inversely proportional to the separation of two electrons, $x_1 - x_2 \approx L$, we expect both Δ_{large} and Δ_{small} to scale as L^{-1}. This is confirmed by measurements of the gap size statistics for MTBs of different lengths ranging from 6 nm to 30 nm (Fig. 5a; this provides further evidence against a Peierls instability-induced gap, which should be length independent). The ratio of E_C/E_0 is thus experimentally observed to be universal for MTBs of different lengths. This ratio is related to TLL behaviour through the TLL parameter K_c as[12,34]

$$K_c = \left(1 + \frac{2E_C}{E_0}\right)^{-\frac{1}{2}} \quad (1)$$

(Supplementary Note 2.1). The energy gaps measured in our spectroscopy of MTBs of different lengths yield a universal value of $K_c = 0.54 \pm 0.03$ (Fig. 5b).

Another piece of evidence supporting the TLL interpretation of MTBs is the observation of spin–charge separation. The existence of

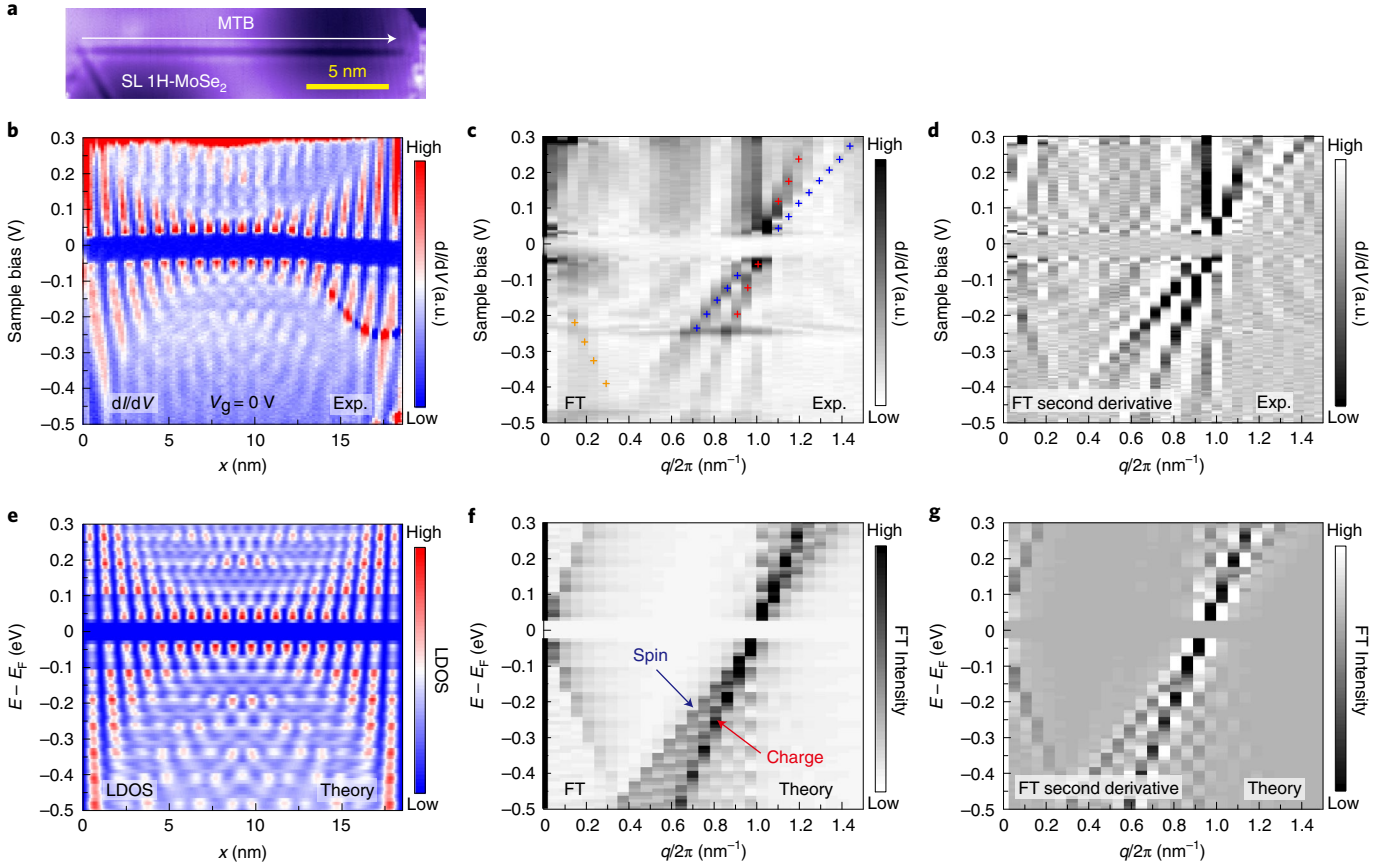

Fig. 4 | Experimental (Exp.) STS along MTB at $V_g = 0$ V compared with theoretical LDOS based on TLL model. a, STM topography of an 18-nm-long MTB ($V_{set} = -2$ V, $I_{set} = 10$ pA). **b**, The d*I*/d*V* intensity plot of the MTB along the white arrow in **a** as a function of sample bias V ($V_{mod} = 5$ mV; tip positioning parameters: $V_{set} = -0.6$ V, $I_{set} = 100$ pA). **c**, FT of the d*I*/d*V* data in **b** as a function of V and wavevector q. Main features include two linear fast branches with different velocities (marked blue and red); a slow branch (orange markers) near the Γ point ($q = 0$); and a static branch with energy-independent wavevector at $q/2\pi \approx 1\,\mathrm{nm}^{-1}$ ($q/2\pi = 2k_F/2\pi$). Enhanced intensity in the horizontal direction at $V \approx -0.25$ V is due to a charging peak in the region $x > 15$ nm in **b**. **d**, The second-derivative plot of FT in **c** enhances the image contrast of the spectral features. **e**, Theoretical LDOS predicted by the finite TLL model using $E_{gap} = 0.08$ eV, $K_c = 0.54$, $K_s = 1$, $k_F^+ = 19\pi/L$, $k_F^- = 18\pi/L$, $v_c\pi/L = 0.073$ eV and $v_s\pi/L = 0.039$ eV. E_{gap} is the energy gap at the Fermi level. K_s is the spin-channel Luttinger parameter. **f**, FT of the theoretical LDOS in **e** shows similar dispersive and static branches as in the experimental data in **c**. **g**, Second-derivative plot of the theoretical FT in **f** for comparison to experimental data in **d**.

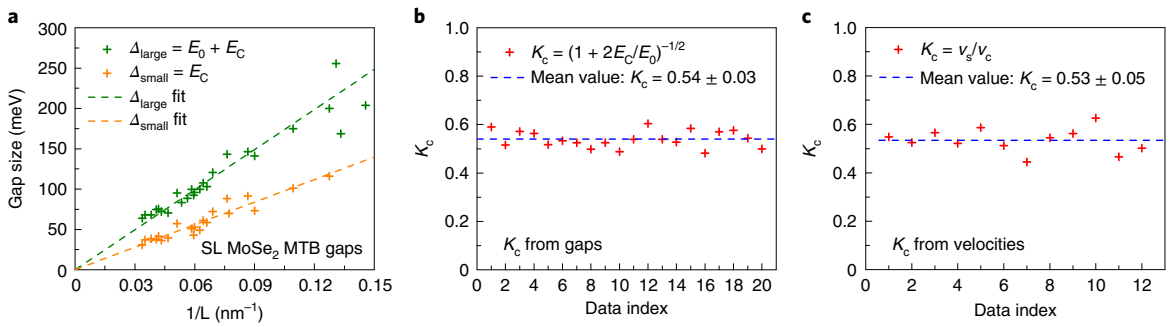

Fig. 5 | Gap size statistics and MTB TLL parameter obtained in two different ways. a, Measured large (green) and small (orange) energy gaps for MTBs of different lengths. Both types of gap scale in size as $1/L$ where L is the MTB length. The dashed lines represent linear fits to the data. **b**, The TLL parameter obtained from the measured charging energy, E_C, and single-particle level spacing, E_0, for MTBs having different lengths ($K_c = 0.54 \pm 0.03$). **c**, The TLL parameter obtained from the ratio of the measured spin and charge velocities for MTBs having different lengths ($K_c = 0.53 \pm 0.05$). The excellent agreement between the K_c values obtained using these two different experimental techniques provides strong evidence for TLL behaviour in SL $MoSe_2$ MTBs.

two linear fast branches in the FT-STS suggests that a single metallic band picture[24,27] for MTBs is insufficient, whereas TLL-based spin–charge separation can explain this behaviour quantitatively. To see this we simulated the expected STM tunnelling LDOS by calculating the electron spectral function for a finite 1D TLL[27,35] having $K_c = 0.54$ (Fig. 4e–g) and with all other material-dependent

parameters constrained by experimental values (Supplementary Note 2.2). Both the fast and slow modulations can be seen in the resulting theoretical energy-dependent LDOS (Fig. 4e), which closely resembles the experimental features seen in Fig. 4b. Clear spin–charge separation can be observed in the FT of the simulated LDOS, as seen in Fig. 4f, where two linear branches show LDOS modulations induced by spin (blue arrow) and charge (red arrow) density excitations that have distinct velocities[27,31,35,36] (the slow branch and static $2k_F$ branch can also both be seen). Direct comparison between Fig. 4c and Fig. 4f allows us to identify the blue and red branches in the experimental data of Fig. 4c as the TLL spin and charge branches, respectively (this can be seen even better by comparing the second-derivative dispersions in Fig. 4d,g). The clear signature of spin–charge separation seen in the FT-STS measurement allows us to experimentally extract the TLL parameter through a second, independent method via the following relation[8,9,15,16,32,33,40]:

$$K_c = \frac{v_s}{v_c}, \quad (2)$$

where v_s and v_c are the slopes (that is, velocities) of the spin and charge branches, respectively (Supplementary Note 2.1). This technique yields a value of $K_c = 0.53 \pm 0.05$ (Fig. 5c), in excellent agreement with the value of $K_c = 0.54 \pm 0.03$ determined from the energy gap ratio E_C/E_0 (Fig. 5b). The TLL picture is thus confirmed through self-consistent measurements of both energy-level alignment (Fig. 2) and spatial LDOS modulations (Fig. 4). We also note that the static modulation, previously interpreted as a Peierls instability[23–26,28], can also be explained by a pure TLL model (Fig. 4f) without invoking the Peierls physics[31,35,36].

In conclusion, our observation of gate-dependent energy gaps via STS allows precise measurement of the el-el Coulomb interaction energy in 1D MTBs. The Luttinger parameter values determined separately from the el-el interaction energy and spin and charge velocities are in excellent agreement with each other. Our device thus provides an ideal platform to study the response of 1D TLL systems to magnetic scatterers[41,42], external magnetic field[43] and tuned dielectric environments[29]. Since the width of MTBs in transition metal dichalcogenides is only ~1 nm, such studies are a critical step towards understanding the behaviour of conducting wires at the ultimate level of miniaturization.

Online content

Any methods, additional references, Nature Research reporting summaries, source data, extended data, supplementary information, acknowledgements, peer review information; details of author contributions and competing interests; and statements of data and code availability are available at https://doi.org/10.1038/s41563-022-01277-3.

Received: 20 August 2021; Accepted: 25 April 2022;
Published online: 16 June 2022

References

1. Kim, B. J. et al. Distinct spinon and holon dispersions in photoemission spectral functions from one-dimensional $SrCuO_2$. *Nat. Phys.* **2**, 397–401 (2006).
2. Grüner, G. The dynamics of charge-density waves. *Rev. Mod. Phys.* **60**, 1129–1181 (1988).
3. Bockrath, M. et al. Single-electron transport in ropes of carbon nanotubes. *Science* **275**, 1922–1925 (1997).
4. Tomonaga, S.-i Remarks on Bloch's method of sound waves applied to many-fermion problems. *Prog. Theor. Phys.* **5**, 544–569 (1950).
5. Luttinger, J. M. An exactly soluble model of a many-fermion system. *J. Math. Phys.* **4**, 1154–1162 (1963).
6. Mattis, D. C. & Lieb, E. H. Exact solution of a many-fermion system and its associated boson field. *J. Math. Phys.* **6**, 304–312 (1965).
7. Haldane, F. D. M. 'Luttinger liquid theory' of one-dimensional quantum fluids. I. Properites of the Luttinger model and their extension to the general 1D interacting spinless Fermi gas. *J. Phys. C* **14**, 2585–2609 (1981).
8. Gogolin, A. O., Nersesyan, A. A. & Tsvelik, A. M. *Bosonization and Strongly Correlated Systems* (Cambridge Univ. Press, 1998).
9. Giamarchi, T. *Quantum Physics in One Dimension* (Oxford Univ. Press, 2004).
10. Matveev, K. A., Furusaki, A. & Glazman, L. I. Bosonization of strongly interacting one-dimensional electrons. *Phys. Rev. B* **76**, 155440 (2007).
11. Ilan, R., Cayssol, J., Bardarson, J. H. & Moore, J. E. Nonequilibrium transport through a gate-controlled barrier on the quantum spin Hall edge. *Phys. Rev. Lett.* **109**, 216602 (2012).
12. Bockrath, M. et al. Luttinger-liquid behaviour in carbon nanotubes. *Nature* **397**, 598–601 (1999).
13. Yao, Z., Postma, H. W. C., Balents, L. & Dekker, C. Carbon nanotube intramolecular junctions. *Nature* **402**, 273–276 (1999).
14. Ishii, H. et al. Direct observation of Tomonaga–Luttinger-liquid state in carbon nanotubes at low temperatures. *Nature* **426**, 540–544 (2003).
15. Lee, J. et al. Real space imaging of one-dimensional standing waves: direct evidence for a Luttinger liquid. *Phys. Rev. Lett.* **93**, 166403 (2004).
16. Shi, Z. et al. Observation of a Luttinger-liquid plasmon in metallic single-walled carbon nanotubes. *Nat. Photon.* **9**, 515–519 (2015).
17. Chang, A. M. Chiral Luttinger liquids at the fractional quantum Hall edge. *Rev. Mod. Phys.* **75**, 1449–1505 (2003).
18. Stühler, R. et al. Tomonaga–Luttinger liquid in the edge channels of a quantum spin Hall insulator. *Nat. Phys.* **16**, 47–51 (2019).
19. Auslaender, O. M. et al. Tunneling spectroscopy of the elementary excitations in a one-dimensional wire. *Science* **295**, 825–828 (2002).
20. Auslaender, O. M. et al. Spin-charge separation and localization in one dimension. *Science* **308**, 88–92 (2005).
21. Jompol, Y. et al. Probing spin-charge separation in a Tomonaga-Luttinger liquid. *Science* **325**, 597–601 (2009).
22. Auslaender, O. M. et al. Experimental evidence for resonant tunneling in a Luttinger liquid. *Phys. Rev. Lett.* **84**, 1764–1767 (2000).
23. Batzill, M. Mirror twin grain boundaries in molybdenum dichalcogenides. *J. Phys. Condens. Matter* **30**, 493001 (2018).
24. Barja, S. et al. Charge density wave order in 1D mirror twin boundaries of single-layer $MoSe_2$. *Nat. Phys.* **12**, 751–757 (2016).
25. Ma, Y. et al. Metallic twin grain boundaries embedded in $MoSe_2$ monolayers grown by molecular beam epitaxy. *ACS Nano* **11**, 5130–5139 (2017).
26. Ma, Y. et al. Angle resolved photoemission spectroscopy reveals spin charge separation in metallic $MoSe_2$ grain boundary. *Nat. Commun.* **8**, 14231 (2017).
27. Jolie, W. et al. Tomonaga-Luttinger liquid in a box: electrons confined within MoS_2 mirror-twin boundaries. *Phys. Rev. X* **9**, 011055 (2019).
28. Wang, L. et al. Direct observation of one-dimensional Peierls-type charge density wave in twin boundaries of monolayer $MoTe_2$. *ACS Nano* **14**, 8299–8306 (2020).
29. Xia, Y. et al. Charge density modulation and the Luttinger liquid state in $MoSe_2$ mirror twin boundaries. *ACS Nano* **14**, 10716–10722 (2020).
30. Yang, X., et al. Manipulating Hubbard-type Coulomb blockade effect of metallic wires embedded in an insulator. Preprint at https://arxiv.org/abs/2104.08577 (2021).
31. Fabrizio, M. & Gogolin, A. O. Interacting one-dimensional electron gas with open boundaries. *Phys. Rev. B* **51**, 17827–17841 (1995).
32. Eggert, S., Johannesson, H. & Mattsson, A. Boundary effects on spectral properties of interacting electrons in one dimension. *Phys. Rev. Lett.* **76**, 1505–1508 (1996).
33. Mattsson, A. E., Eggert, S. & Johannesson, H. Properties of a Luttinger liquid with boundaries at finite temperature and size. *Phys. Rev. B* **56**, 15615–15628 (1997).
34. Kane, C., Balents, L. & Fisher, M. P. A. Coulomb interactions and mesoscopic effects in carbon nanotubes. *Phys. Rev. Lett.* **79**, 5086–5089 (1997).
35. Anfuso, F. & Eggert, S. Luttinger liquid in a finite one-dimensional wire with box-like boundary conditions. *Phys. Rev. B* **68**, 241301 (2003).
36. Kakashvili, P., Johannesson, H. & Eggert, S. Local spectral weight of a Luttinger liquid: effects from edges and impurities. *Phys. Rev. B* **74**, 085114 (2006).
37. Yang, W. et al. Epitaxial growth of single-domain graphene on hexagonal boron nitride. *Nat. Mater.* **12**, 792–797 (2013).
38. Brar, V. W. et al. Gate-controlled ionization and screening of cobalt adatoms on a graphene surface. *Nat. Phys.* **7**, 43–47 (2011).
39. Mallet, P., Sacks, W., Roditchev, D., Défourneau, D. & Klein, J. Spatial and energy variation of the local density of states in the charge density wave phase of 2H–$NbSe_2$. *J. Vac. Sci. Technol. B* **14**, 1070–1074 (1996).
40. Miranda, E. Introduction to bosonization. *Braz. J. Phys.* **33**, 3–35 (2003).
41. Lee, D. H. & Toner, J. Kondo effect in a Luttinger liquid. *Phys. Rev. Lett.* **69**, 3378–3381 (1992).
42. Furusaki, A. & Nagaosa, N. Kondo effect in a Tomonaga-Luttinger liquid. *Phys. Rev. Lett.* **72**, 892–895 (1994).
43. Hikihara, T., Furusaki, A. & Matveev, K. A. Renormalization of impurity scattering in one-dimensional interacting electron systems in magnetic field. *Phys. Rev. B* **72**, 035301 (2005).

Methods

Sample fabrication. The preparation of the epitaxial graphene/hBN heterostructure supported on a SiO_2/Si substrate is described in ref. [37]. Single-layer 1H-$MoSe_2$ films with MTBs were grown directly on epitaxial graphene/hBN heterostructures using MBE. Mo and Se were evaporated from an electron-beam evaporator and a home-built Knudsen cell, respectively. The flux ratio between Mo and Se was ~1:100 and the sample was kept at 450 °C during the growth. After growth the sample was heated to ~600 °C and annealed under Se for 30 min. The sample was capped with ~20 nm of amorphous Se before being taken out of the ultra-high-vacuum growth chamber. Electrical contacts were made by depositing Cr and Au (3 nm and 30 nm) through a shadow mask.

STM/STS measurements. STM/STS measurements were performed in a low-temperature ultra-high-vacuum STM system (CreaTec) at $T = 5$ K. Prior to measurement, the samples were annealed in ultra-high vacuum at ~200 °C for 1 hour to remove the Se capping layers and then immediately transferred in situ to the STM stage at $T = 5$ K. Electrochemically etched tungsten tips were calibrated on a Au(111) surface before other measurements. The dI/dV spectra were collected using standard lock-in techniques (frequency $f = 401$ Hz). The dI/dV mapping was performed in constant-height mode (that is, with the feedback loop open).

Data availability

The data that support the findings of this study are available from the corresponding authors upon reasonable request. Source data are provided with this paper.

Code availability

The codes used in this study are available from the corresponding authors upon reasonable request.

Acknowledgements

This research was supported as part of the Center for Novel Pathways to Quantum Coherence in Materials, an Energy Frontier Research Center funded by the US Department of Energy, Office of Science, Basic Energy Sciences (material growth, STM spectroscopy, theoretical simulations). Support was also provided by the National Science Foundation through grant DMR-1807233 (device design). S.W. and G.Z. acknowledge support by Guangdong Basic and Applied Basic Research Foundation through grant no. 2019A1515110898 (epitaxial graphene growth). Z.Q.Q. acknowledges support by the National Research Foundation of Korea through grant no. 2015M3D1A1070467 (MBE instrumentation development) and no. 2015R1A5A1009962 (MBE growth characterization). K.W. and T.T. acknowledge support from the Elemental Strategy Initiative conducted by the Ministry of Education, Culture, Sports, Science and Technology, Japan, grant no. JPMXP0112101001 (hBN growth) and the Japan Society for the Promotion of Science KAKENHI grant no. 19H05790 (hBN characterization) and no. JP20H00354 (development of new hBN growth tools).

Author contributions

T.Z., W.R., F.W. and M.F.C. initiated and conceived this project. W.R., T.Z. and C.Z. carried out STM/STS measurements under the supervision of M.F.C.; Y.-Q.W. and W.R. performed theoretical analysis and numerical calculation under the supervision of J.E.M.; T.Z. and T.W. performed MBE growth under the supervision of Z.Q.Q.; H.-Z.T. and F.L. performed device fabrication under the supervision of M.F.C. and A.Z.; S.W. prepared epitaxial graphene under the supervision of G.Z.; and K.W. and T.T. synthesized hBN crystals. T.Z., W.R., J.B.N., A.W.-B., F.W. and M.F.C. analysed the experimental data. T.Z., W.R., Y.-Q.W. and M.F.C. wrote the manuscript with help from all the authors. All authors contributed to the scientific discussion.

Competing interests

The authors declare no competing interests.

Additional information

Supplementary information The online version contains supplementary material available at https://doi.org/10.1038/s41563-022-01277-3.

Correspondence and requests for materials should be addressed to Wei Ruan, Feng Wang, Joel E. Moore or Michael F. Crommie.

Peer review information *Nature Materials* thanks the anonymous reviewers for their contribution to the peer review of this work.